JGR Oceans

RESEARCH ARTICLE
10.1029/2019JC015228

Enhanced Energy Dissipation in the Equatorial Pycnocline by Wind-Induced Internal Wave Activity

A. Natarov[1] **and K. J. Richards**[1,2]

[1]International Pacific Research Center, University of Hawai'i at Mānoa, Honolulu, HI, USA, [2]Department of Oceanography, University of Hawai'i at Mānoa, Honolulu, HI, USA

Key Points:
- Enhanced energy dissipation occurs close to the equator independently of the geographical distribution of wind forcing
- The most important process in enhancing mixing in the ocean interior is wave action convergence at the turning latitudes
- Other mechanism (nonlinear wave-wave interactions and refraction through pycnocline) may be important under certain conditions

Correspondence to:
A. Natarov,
natarov@hawaii.edu

Citation:
Natarov, A., & Richards, K. J. (2019). Enhanced energy dissipation in the equatorial pycnocline by wind-induced internal wave activity. *Journal of Geophysical Research: Oceans*, *124*, 6200–6217. https://doi.org/10.1029/2019JC015228

Received 16 APR 2019
Accepted 7 AUG 2019
Accepted article online 12 AUG 2019
Published online 27 AUG 2019

Abstract Numerical experiments show that in a zonally symmetric model of a tropical ocean forced only by transient winds both inertia-gravity wave activity and the energy dissipation rate have a pronounced maximum in the pycnocline close to the equator regardless of the latitudinal distribution of the energy input into the ocean's mixed layer. We consider a number of factors that determine the spatial distribution of mixing and find that equatorial enhancement is due to a combination of three factors: a stronger superinertial component of the wind forcing close to the equator, wave action convergence at turning latitudes for equatorially trapped waves, and nonlinear wave-wave interactions between equatorially trapped waves. The most important factor is wave action convergence at turning latitudes.

1. Introduction

Ocean mixing plays a very important role in climate dynamics on time scales ranging from a few weeks to many decades. The processes that cause mixing, however, are generally not resolved in climate models or even stand-alone oceanic general circulation models. It is therefore important to connect these processes to resolvable large-scale dynamics, so that mixing can be accounted for correctly in simulations. While the mixing processes that dominate in the unstratified mixed layer (i.e., mixing due to momentum and buoyancy fluxes at the air-sea interface) are relatively well understood, mixing processes that occur in the ocean interior away from the boundaries are not. These form the focus of this study.

To keep the experiments computationally inexpensive and the dynamics amenable to simple analysis, we only consider a zonally symmetric setting in which there is no variation in the east-west direction. Let the state of the ocean be characterized by the free surface elevation $\zeta(y,t)$, density field $\rho(y,z,t)$, and three-dimensional velocity field $\mathbf{v}(y,z,t) = [\mathbf{u}, w](y,z,t)$, where $\mathbf{u}$ is the horizontal and w is the vertical components of the velocity vector, y is the meridional (northward) coordinate, z is the vertical (upward) coordinate, and t is time. Let ρ_* be some constant reference density close to the mean density of the fluid and g be the gravitational acceleration. To simplify the equations, it is useful to introduce the buoyancy field $b(y,z,t) = -(g/\rho_*)\rho(y,z,t)$. Mixing in the interior is believed to be primarily caused by dynamic instabilities similar to those that occur in steady parallel shear flows when the vertical shear of the horizontal flow $S^2 = |\partial\mathbf{u}/\partial z|^2$ exceeds the buoyancy frequency $N^2 = \partial b/\partial z$ by more than a factor of 4 or, in other words, when the Richardson number $Ri = N^2/S^2$ is less than a quarter (Howard, 1961; Miles, 1961). If a similar stability criterion holds for more complex time-dependent flows, then interior mixing in the ocean should be associated with features that have a small vertical scale and a relatively large velocity magnitude. We will refer to such features as *small vertical scale* features, or *SVSs* (cf. Natarov & Richards, 2015). In situ observations, such as high-resolution profiles of the horizontal velocity and kinetic energy dissipation rate, suggest that levels of mixing are indeed correlated with the levels of SVS activity, at least at depths above 300 m in the western equatorial Pacific Ocean (Richards et al., 2012, 2015) and elsewhere in the equatorial ocean (cf. Gregg et al., 1985; Moum et al., 1989).

Theoretical and modeling studies show that the two major sources of SVSs are instabilities of swift equatorial currents (Natarov et al., 2008; Natarov & Richards, 2009, 2015) and oscillations in the mixed layer that occur after strong transient wind events (cf. D'Asaro, 1989; Gill, 1984). Away from the equator such oscillations in the mixed layer are called near-inertial oscillations: Their frequency is set by the value of the local Coriolis parameter f; the only frequency at which free oscillations can exist in an unstratified mixed layer under

the hydrostatic approximation. As near-inertial oscillations modulate the depth of the base of the mixed layer, they induce inertial pumping (Gill, 1984) and radiate energy into the ocean interior in the form of near-inertial waves (NIWs) that propagate both vertically and horizontally. However, close to the equator the inertial period becomes very long, and it is interesting to assess whether the inertial pumping scenario still adequately describes the main mechanism of internal wave generation.

In this study we focus on SVSs and mixing produced by transient winds. In section 2 we describe a simple zonally symmetric tropical ocean model. The connection between the inertia-gravity wave (IGW) activity and kinetic energy dissipation inferred from parameterized vertical eddy diffusivity in model integrations are discussed in section 3. One puzzling phenomenon observed in our simulations is the confinement of the elevated levels of both IGW activity and kinetic energy dissipation rate to the vicinity of the equator even in the case when the largest input of wind energy occurs far away from the equator. In section 4 we examine various hypotheses that may explain the equatorial enhancement of SVS activity and kinetic energy dissipation using ray tracing and wave action conservation. To further test the proposed mechanisms in a more controlled setting, we conduct a series of idealized wind burst experiments. The main findings are summarized and discussed in section 5.

2. Ocean Model

We study the evolution of a stratified flow on the equatorial β plane. The fluid is assumed to be incompressible and governed by the Boussinesq approximation (Vallis, 2006):

$$\frac{\partial \mathbf{v}}{\partial t} = -\mathbf{v}\cdot\nabla\mathbf{v} - \mathbf{f}\times\mathbf{v} - \nabla\phi + b\hat{\mathbf{k}} + \nu\nabla^2\mathbf{v} + \mathcal{D}_{\mathbf{v}} \tag{1a}$$

$$\frac{\partial T}{\partial t} = -\mathbf{v}\cdot\nabla T + \kappa_T\nabla^2 T + \mathcal{D}_T, \tag{1b}$$

$$\nabla\cdot\mathbf{v} = 0, \tag{1c}$$

$$b = b_* + \alpha(T - T_*), \tag{1d}$$

where $\mathbf{v}$ denotes velocity, $\mathbf{f} = [0, 0, \beta y]$ is the Coriolis parameter, $\phi = p/\rho_*$ is the geopotential (and p is pressure), $b_{(*)}$ is the (reference) buoyancy, $\hat{\mathbf{k}}$ is the unit vector in the direction of the increasing vertical coordinate, $T_{(*)}$ is the (reference) temperature, α is the thermal expansion coefficient of the sea water, $\{\nu, \kappa_T\}$ are the molecular {momentum, temperature} diffusivities, and $\mathcal{D}_{(\cdot)}$ represents fluxes due to unresolved processes (including but, in general, not confined to turbulence). The spatial coordinates are y (oriented from south to north) and z (bottom to top). The equations are solved on a model domain which is 4,000 km wide in the meridional direction and is centered on the equator. No-flux boundary conditions are imposed at the northern and southern boundaries. The ocean bottom is placed at a uniform depth of 1,000 m.

To filter out double-diffusive processes and complications due to the nonlinearity of the equation of state, we chose the equation of state to be linear and a function of temperature alone. The governing equations can therefore be written as

$$\frac{\partial \mathbf{v}}{\partial t} = -\mathbf{v}\cdot\nabla\mathbf{v} - \mathbf{f}\times\mathbf{v} - \nabla\phi + b\hat{\mathbf{k}} + \nu\nabla^2\mathbf{v} + \mathcal{D}_{\mathbf{v}} \tag{2a}$$

$$\frac{\partial b}{\partial t} = -\mathbf{v}\cdot\nabla b + \kappa_b\nabla^2 b + \mathcal{D}_b, \tag{2b}$$

$$\nabla\cdot\mathbf{v} = 0, \tag{2c}$$

where $\kappa_b = \alpha\kappa_T$ is the molecular diffusion coefficient for buoyancy and $\mathcal{D}_b$ is the buoyancy flux due to unresolved processes. We s et all molecular diffusion coefficients to 0, so that all dissipation and diffusion that occur in the model is due to the unresolved, parameterized processes to be discussed shortly.

The initial stratification profile is shown in Figure 1 (the initial buoyancy field is independent of y). From top to bottom it consists of the surface mixed layer (the upper 20 m) separated by a sharp density jump from a weakly stratified transition layer between 20 and 200-m depths, pycnocline (between 200 and

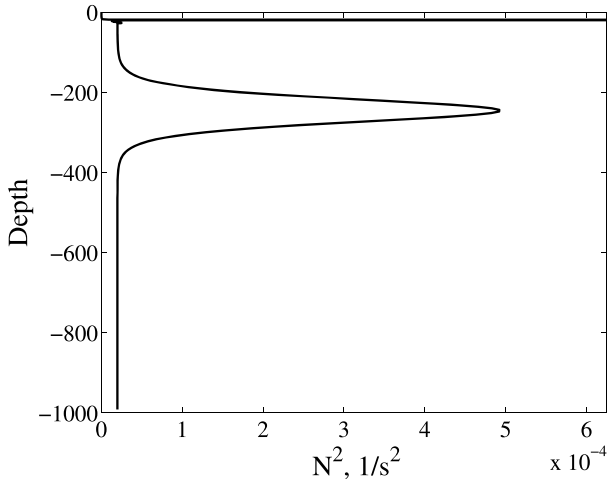

Figure 1. The initial background buoyancy frequency profile used in the numerical experiments.

300 m), and weakly stratified subpycnocline (between 300 to 1,000 m). Similar stratification often occurs in the western equatorial Pacific Ocean (cf. Richards et al., 2012).

The only forcing in the model is the wind stress. To construct the forcing, we use the ERA-interim wind product. It has temporal resolution of 6 hr and horizontal resolution of approximately 125 km. The wind stress field $\vec{\tau}$ is estimated from the wind velocity at 10-m height, $\mathbf{U}_{10\mathrm{m}} = [U_{10\mathrm{m}}, V_{10\mathrm{m}}]$ using the parameterization

$$\vec{\tau} = \rho_{\mathrm{air}} c_d \left|\mathbf{U}_{10\mathrm{m}}\right| \mathbf{U}_{10\mathrm{m}}, \tag{3}$$

where $\rho_{\mathrm{air}} = 1.3\ \mathrm{kg/m^3}$ is the density of air and $c_d = \left(0.44 + 0.063\,\mathrm{m^{-1}\cdot s^{-1}}\left|\mathbf{U}_{10\mathrm{m}}\right|\right) \times 10^{-3}$ is the drag coefficient (Stewart, 2005). If the wind stress had a steady component, a zonally symmetric model would develop unrealistically strong currents (cf. McCreary, 1981). To circumvent this problem, we remove the temporal mean over the model integration period from the forcing.

In each case the model is run for 244 days, which appears to be a sufficient amount of time necessary for the IGWs to populate the ocean interior. Experiments are conducted for two periods: 1 April to 30 November 2008 (Period I) and 1 January to 31 August 2007 (Period II). For Period I the strongest transient winds occur primarily on the equator, whereas for Period II the strongest winds are observed in the Southern Hemisphere well off the equator.

To carry out the numerical experiments, we use the Regional Ocean Modeling System (ROMS; Shchepetkin & McWilliams, 2005) with 4-km resolution in the meridional direction. ROMS is a σ coordinate model, and our vertical resolution varies from 0.8 m in the upper layers to 8 m at the bottom. The resolution in the pycnocline ranges from 3.7 to 4.3 m, and the model has 25σ levels between 200- and 300-m depths.

To mimic the underresolved Kelvin-Helmholtz instability that may occur within a given grid cell, we turn on a turbulent mixing parameterization scheme of a type proposed by Large et al. (1994), which consists of adding a vertical eddy diffusivity coefficient ν_{eddy} to the background second-order vertical viscosity and diffusion coefficients (see values for ν_b and κ_b in Table 1). The eddy viscosity coefficient is given by

$$\nu_{\mathrm{eddy}} = \nu_0\left[1 - (4Ri)^2\right]^3, \tag{4}$$

whenever the local instantaneous Richardson number $Ri = b_z / \left(\mathbf{u}_z \cdot \mathbf{u}_z\right)$ drops below 1/4. Both the turbulent eddy viscosity and diffusivity are modeled using this mixing parameterization scheme, which is essentially a modified k-profile parameterization (KPP) scheme with parameters more appropriate to our model resolution. The value of the horizontal viscosity ν_h is set to 5 $\mathrm{m^2/s^2}$. To ensure numerical stability at subgrid scales, we also use a fourth-order horizontal hyperviscosity with the coefficient $\nu_{4,h}$ equal to 10^{10} $\mathrm{m^4/s}$. These and other parameters are listed in Table 1.

In the mixed layer, the eddy diffusivity coefficient is parameterized using the semiempirical Monin-Obukhov similarity theory, as described in Large et al. (1994). The general formulation involves surface buoyancy flux

Table 1
Parameters Used in the Numerical Experiments Using ROMS

Parameter	Notation	Value	Units
grav. acceleration	g	9.78	$\mathrm{m/s^2}$
Coriolis parameter gradient	β	2.28×10^{-11}	$\mathrm{m^{-1}\cdot s^{-1}}$
Background vert. viscosity	ν_b	0	$\mathrm{m^2/s}$
Background vert. diffusivity	κ_b	0	$\mathrm{m^2/s}$
Max. vert. eddy viscosity	ν_0	10^{-3}	$\mathrm{m^2/s}$
Max. vert. eddy diffusivity	κ_0	10^{-3}	$\mathrm{m^2/s}$
Horizontal viscosity	ν_h	5	$\mathrm{m^2/s}$
Horizontal hyperviscosity	ν_4	10^{10}	$\mathrm{m^4/s}$

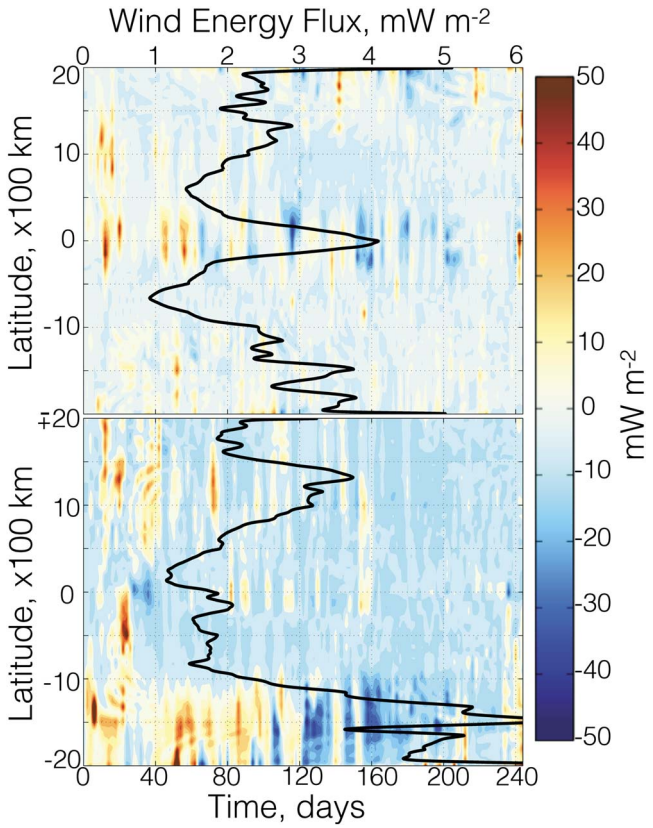

Figure 2. Wind energy flux into the ocean as a function of time and latitude (contour plots) and its temporal average (solid black lines). The upper panel corresponds to Period I (from 1 April to 30 November 2008), and the lower panel corresponds to Period II (from 1 January to 30 August 2007). During Period I most of the wind energy input into the ocean occurs close to the equator, whereas during Period II most of the wind energy input occurs in the Southern Hemisphere.

B_f , which is 0 in our study. Therefore, the actual parameterization that we use can be described as follows. First, the depth of the mixed layer base, $z_{m\ell}$, is determined as the minimum between the Ekman depth z_E and the shallowest depth $z_{Ri_b<1/4}$ at which the bulk Richardson number Ri_b becomes critical, that is, drops below 1/4:

$$z_{m\ell} = \min\left\{z_E, z_{Ri_b<1/4}\right\}. \tag{5}$$

The Ekman depth is given by $z_E = 0.7u_*/f$, where

$$u_* = \frac{|\vec{\tau}|}{\rho_*} \tag{6}$$

is the friction velocity.

The bulk Richardson number is defined as

$$Ri_b = \frac{(\langle b\rangle - b)\,|\zeta - z|}{|\langle \mathbf{u}\rangle - \mathbf{u}|^2}, \tag{7}$$

where ζ is the free surface elevation and $\langle\cdot\rangle$ denotes the average over the upper 10% of the mixed layer depth.

The eddy diffusivity above $z_{m\ell}$ is then calculated using

$$\nu = (\zeta - z_{m\ell})\, w_* \left(\frac{\zeta - z}{\zeta - z_{m\ell}}\right) G\left(\frac{\zeta - z}{\zeta - z_{m\ell}}\right), \tag{8}$$

where w_* is the turbulent vertical velocity and G is an empirical nondimensional shape function with a free parameter that allows it to match the eddy viscosity just below the base of the mixed layer depth $z_{m\ell}$.

3. Experiments

3.1. Energy Balance

As discussed in the previous section, the only forcing in our model is the wind stress with a zero temporal mean. Figure 2 shows the rate of wind energy input into the mixed layer (i.e., $\dot{W} = \vec{\tau} \cdot \mathbf{v}_s$, where $\dot{W}$ denotes the rate of wind work per unit of free surface area, $\vec{\tau} = [\tau_x, \tau_y]$ is the wind stress vector, and $\mathbf{v}_s$ is the ocean velocity vector at the free surface) during Periods I and II. Input of energy into the ocean occurs via energetic wind bursts each lasting a few days. The wind bursts are meridionally coherent over a horizontal scale of several hundred kilometers and the wind energy flux into the ocean can reach values up to 50 mW/m^2. While the wind stress itself has zero temporal mean in our setting, the total wind work over the integration period does not: The time-averaged wind input has a maximum close to the equator during Period I and in the Southern Hemisphere during Period II, as shown by solid black lines in Figure 2. For this reason we will also refer to Period I as the "equatorial wind" and Period II as the "off-equatorial wind" cases below.

Interestingly, averaged over time and latitude, the wind energy flux into the ocean is approximately 2.7 mW/m^2 for both the equatorial and off-equatorial wind cases. Integrated over 244 days, the wind pumps into the ocean approximately 57 kJ of energy per square meter of the horizontal surface area. To determine the partition of this energy between the mixed layer and ocean interior, as well as to make some progress toward estimating the rate of emission of IGW energy from the mixed layer into the ocean interior, we proceed as follows. The total energy density field for the Boussinesq fluid under the hydrostatic approximation is given by

$$E(\mathbf{x}, t) = K(\mathbf{x}, t) + P(\mathbf{x}, t), \tag{9}$$

where

$$K = \frac{1}{2}\rho_* \mathbf{u} \cdot \mathbf{u} \tag{10}$$

is the kinetic and

$$P = \rho g z \tag{11}$$

is the potential energy density. The balance for the total energy density field, $E(\mathbf{x}, t)$, can be written as

$$\frac{\partial E}{\partial t} + \nabla_h \cdot \mathbf{F}_h + \frac{\partial F_v}{\partial z} = G_E + D_E, \tag{12}$$

where subscript h denotes horizontal components and subscript v stands for the vertical component of the vector field, so that we can write the spatial coordinate as $\mathbf{x} = [\mathbf{x}_h, z]$, and the total energy density flux vector as $\mathbf{F} = \left[\mathbf{F}_h, F_v\right]$. The terms G_E and D_E on the right-hand side represent generating sources and dissipating sinks, respectively. Energy density dissipation, D_E, can be partitioned into dissipation due to horizontal and vertical viscosity, with

$$D_E = D_h + D_v. \tag{13}$$

The energy density flux vector is given by

$$\mathbf{F} = \mathbf{v}\,(E + p)\,. \tag{14}$$

It is convenient for our purposes to partition the total energy of the system into the energy contained in the mixed layer, $E_{m\ell}$, and in the ocean interior, E_{int}, where

$$E_{m\ell}\left(\mathbf{x}_h, t\right) = \int_{z_{m\ell}}^{\zeta} \mathrm{d}z E\left(\mathbf{x}_h, z, t\right), \tag{15a}$$

$$E_{\text{int}}\left(\mathbf{x}_h, t\right) = \int_{-H}^{z_{m\ell}} \mathrm{d}z E\left(\mathbf{x}_h, z, t\right). \tag{15b}$$

The fields $E_{m\ell}$ and E_{int} have units of energy per unit area. A similar decomposition can be performed separately for K, P, $\mathbf{F}$, D_h, and D_v to construct horizontal densities of various types of energy (i.e., kinetic, potential, flux, horizontal dissipation, and vertical dissipation).

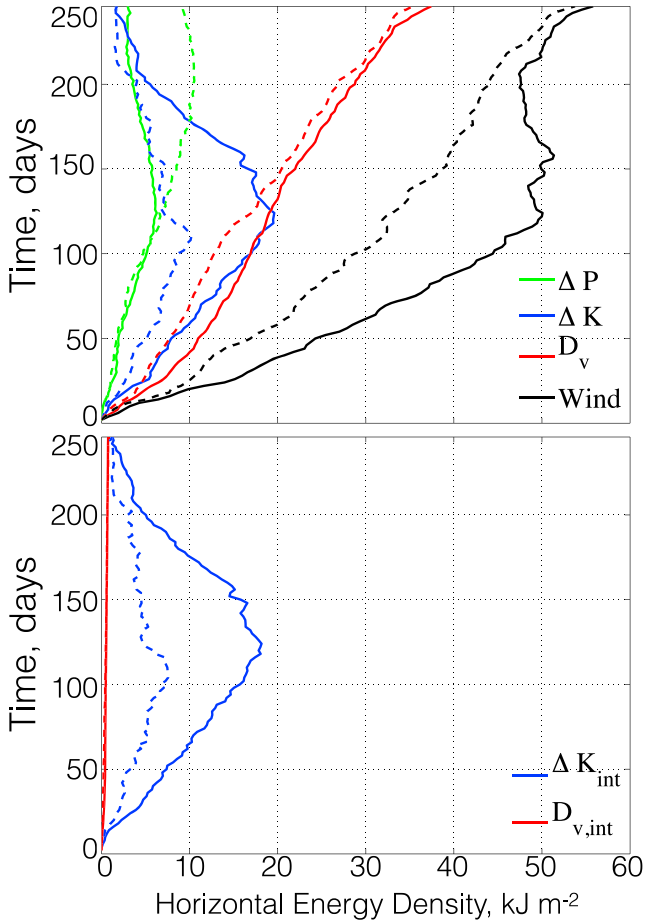

Figure 3. Total energy partition as a function of time. The upper panel shows the horizontal energy density through the entire ocean depth; the lower panel shows horizontal densities in the ocean interior (i.e., below the mixed layer). Dashed lines correspond to Period I (equatorial wind), and solid lines corresponds to Period II (off-equatorial wind). Ocean interior contains almost all mechanical energy in the system (blue lines represent the kinetic energy and green lines represent the potential energy), but most energy dissipation due to vertical mixing (red) occurs in the mixed layer.

Let $\Delta\phi(t)$ denote the difference between a quantity ϕ at time t and its initial value. The change with time in total energy and its partition between changes in kinetic energy, ΔK, potential energy, ΔP, and cumulative vertical dissipation D_v are shown in Figure 3. Also shown is the wind work denoted by "Wind". The upper panel shows energies integrated over the entire ocean depth, and the lower panel shows the kinetic energy and its dissipation due to vertical mixing in the ocean interior (i.e., below the base of the mixed layer). Dashed lines correspond to equatorial winds, and solid lines correspond to off-equatorial winds. Note that while the ocean interior contains most of the kinetic energy, most dissipation takes place in the mixed layer. Energy dissipation in the ocean interior plays a minor role in the overall energy balance.

The maximum kinetic energy is achieved in the middle of the integration for both periods. After that the ocean is losing kinetic energy. Because the mean winds have been removed from the system, average forcing is zero at each latitude. However, there is irreversible energy dissipation, with most energy dissipating through vertical mixing in the mixed layer. Energy is also removed through negative wind energy flux close to the equator during Period I and in the Southern Hemisphere during Period II. Almost all dissipation due to horizontal mixing is due to hyperviscosity (not shown), and the results are therefore not unduly sensitive to the choice of the horizontal viscosity coefficient ν_h.

3.2. Eddy Viscosity

We assume that the magnitude of the eddy viscosity coefficient at each point in space and time reflects the rate of energy dissipation at that point. The distribution of base-10 logarithm of the eddy viscosity coefficient below the mixed layer, averaged over the integration period, is shown in Figure 4. Surprisingly, the interior

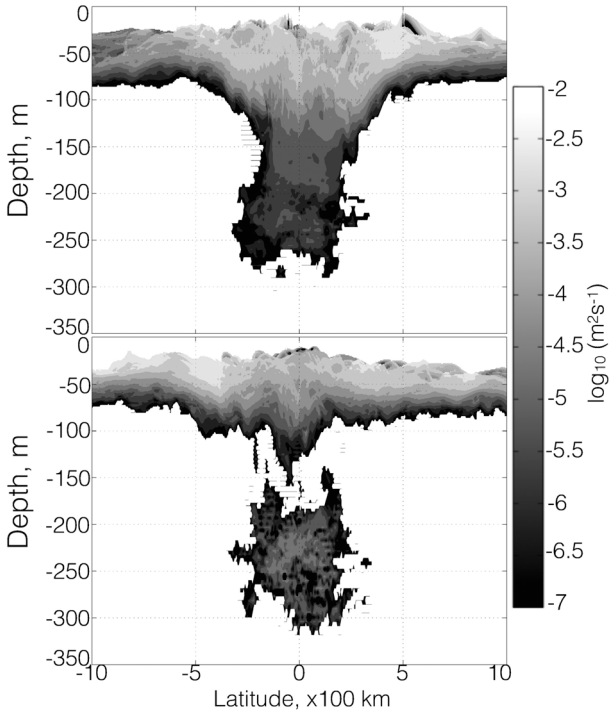

Figure 4. Base-10 logarithm of time-averaged vertical eddy viscosity coefficient below the mixed layer. (upper panel) Period I (equatorial winds). (lower panel) Period II (off-equatorial winds).

dissipation in the pycnocline is confined to the proximity of the equator for both on- and off-equatorial winds. Strong dissipation just below the mixed layer is more spread out meridionally in both experiments, although even here enhanced dissipation extends deeper into the transition layer close to the equator. As we show in section 4.3, mixing in the transition layer close to the equator is due to the Yoshida jet driven by the convergence of Ekman transport in the mixed layer on the equator and is considerably more enhanced in the equatorial winds case than in the off-equatorial winds case.

3.3. Froude Number

As described in section 2, the interior eddy viscosity coefficient in our model is a function of the Richardson number Ri, or its inverse, the Froude number squared Fr^2. The upper panel of Figure 5 shows the snapshot of the Froude number squared on Day 244, and the lower panel shows the temporal average of the Froude number over the integration period for the off-equatorial wind case. In addition to high values of the Froude number in the equatorial pycnocline as already conveyed by Figure 4, we also find relatively high Fr^2 values everywhere just below the mixed layer and below the pycnocline close to the equator. Note that scales associated with patches of high Froude number are much smaller in both vertical and horizontal directions in the snapshot than in the temporal mean. This is consistent with the generation of turbulence in the ocean interior being associated with SVSs. As we show in section 4.2, most SVSs in Figure 5 originate as IGW beams emanating from the base of the mixed layer and initially propagating toward the equator at a well-defined angle in the (y, z) plane. Just below the base of the mixed layer, the Froude number squared associated with each IGW beam exceeds the critical value of four but quickly decreases with depth in the transition layer. The Froude number amplifies once the beam enters the pycnocline. In section 4.2 we use ray tracing to describe changes to the vertical component of the wave vector, wave energy density, and Froude number as wave packets enter the pycnocline (depths between 200 and 300 m).

Another important feature of the solution is high values of the Froude number at some depths below the pycnocline close to the equator. This suggests that equatorial trapping plays an important role in the distribution of the energy dissipation, and this is examined in section 4.2. The Froude number amplification in this case occurs through convergence of wave action at turning latitudes.

Finally, we cannot rule out nonlinear wave-wave interactions from playing a role in the enhancement of energy dissipation close to the equator. Vertical scales much smaller than those produced by linear dynamics can be generated through parametric subharmonic instability (PSI; cf. d'Orgeville & Hua, 2005; Natarov et al., 2008) and other types of nonlinear wave-wave interactions (cf. McComas & Bretherton, 1977; Staquet & Sommeria, 2002; Sun & Kunze, 1999) . We argue that the nonlinear cascade to SVSs is indeed manifested in our simulations in section 4.3, where we also show the importance of the Yoshida jet in driving high levels of mixing in the transition layer in the immediate proximity of the equator.

3.4. Subinertial and Superinertial Components of the Wind Stress

To better understand the role of wind forcing in determining the spatial distribution of energy dissipation, we take a closer look at the temporal spectrum characteristics of the wind stress. The temporal resolution of the wind stress forcing is $(\Delta t)_\tau = 6$ hr and the duration of the model integration period is $T = 244$ days. The temporal wind stress spectrum and its spectral power density distribution in (ω, y) space are

$$\tau(\omega, y) = \frac{1}{T}\int_0^T \mathrm{d}t\ \tau(t, y)\exp(-i\omega t)\,, \tag{16a}$$

$$P[\tau](\omega, y) = \tau^*(\omega, y)\tau(\omega, y), \tag{16b}$$

respectively, where τ can be either τ_x or τ_y, * denotes complex conjugation, for a discrete set of frequencies $\omega_j = 2\pi j/T, j = -J_\tau, -J_\tau + 1, \ldots, J_\tau - 1, J_\tau$, where $J_\tau = T/(2(\Delta t)_\tau)$.

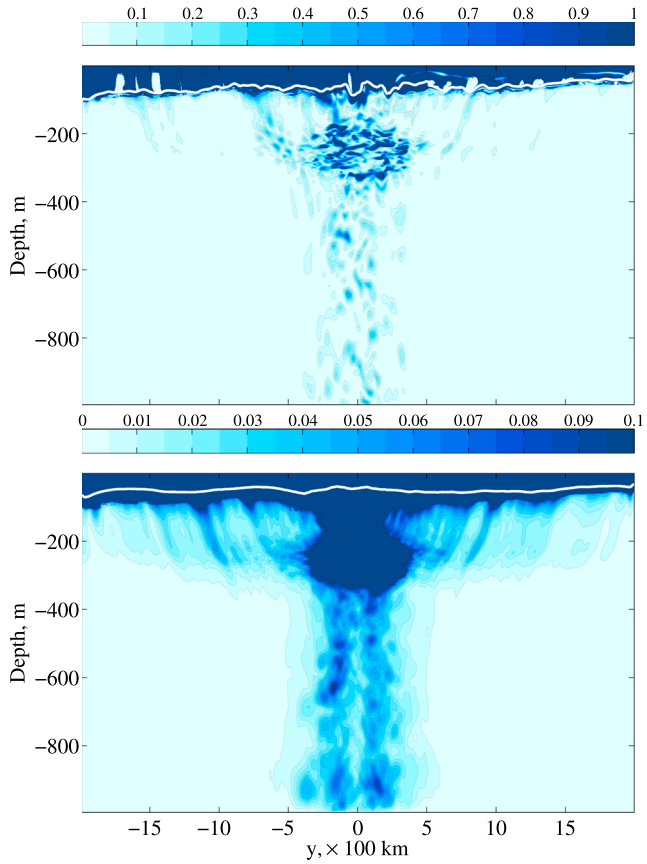

Figure 5. A snapshot (the upper panel) and time-averaged (lower panel) Froude number in the off-equatorial wind experiment. The snapshot is taken on the last day of the model integration period (Day 244). The amplification of the Froude number in the pycnocline (depths between 200 and 300 m) is evident in both figures.

The frequency of IGWs is limited from below by the absolute value of the local Coriolis parameter, $|f|$. The total wind stress τ can be decomposed into subinertial and superinertial components; that is, $\tau = \tau_{|\omega| \le |f|} + \tau_{|\omega|>|f|}$, and linear theory suggests that only the superinertial component $\tau_{|\omega|>|f|}$ can generate IGWs propagating into the ocean interior at a meridional location $y = f/\beta$.

The temporal spectra of the zonal component of the wind stress, $P\left[\tau_x\right](\omega, y)$ for both periods are shown in Figure 6. Instead of frequencies, we label the locations along the horizontal axis by the periods to which these spectral components correspond. There is a relatively weak local maximum at the diurnal and highest resolvable semidiurnal frequencies at most meridional locations, but overall the spectrum is very red and almost all power is contained at low frequencies. The blue color scale in Figure 6 is strongly saturated to enhance visibility of the features at high frequencies.

Because the absolute value of the local inertial frequency, $f = \beta y$, increases with distance from the equator, the lower boundary of the spectral range for superinertial forcing is also increasing and the superinertial component of the wind stress decays fast with the distance away from the equator. Therefore, even when the magnitude of the wind stress is largest south of the equator, such as in the off-equatorial wind case (the lower panel in Figure 6), the superinertial contribution remains largest close to the equator. The integrated power spectrum of the superinertial wind stress, $P\left[\tau_{|\omega|\ge|f|}\right](y) = (2\pi)^{-1}\int_{|\omega|\ge|f|} d\omega\ P\left[\tau_x\right](\omega, y)$, normalized by the maximum over all frequencies, latitudes, and both periods, is represented by red lines. In both on- and off-equatorial cases it is strongly peaked at the equator. At higher latitudes the total wind power input is not necessarily weaker than at the equator, but most of the wind energy goes into quasi-steady currents instead of IGWs. Unlike IGWs, the quasi-steady currents do not experience reduction in horizontal and vertical scales due to β dispersion and do not propagate meridionally toward the equator, as evident in plots of the mixed layer kinetic energy, $K_{m\ell}$, as a function of latitude and time (not shown). In section 4.3 we describe

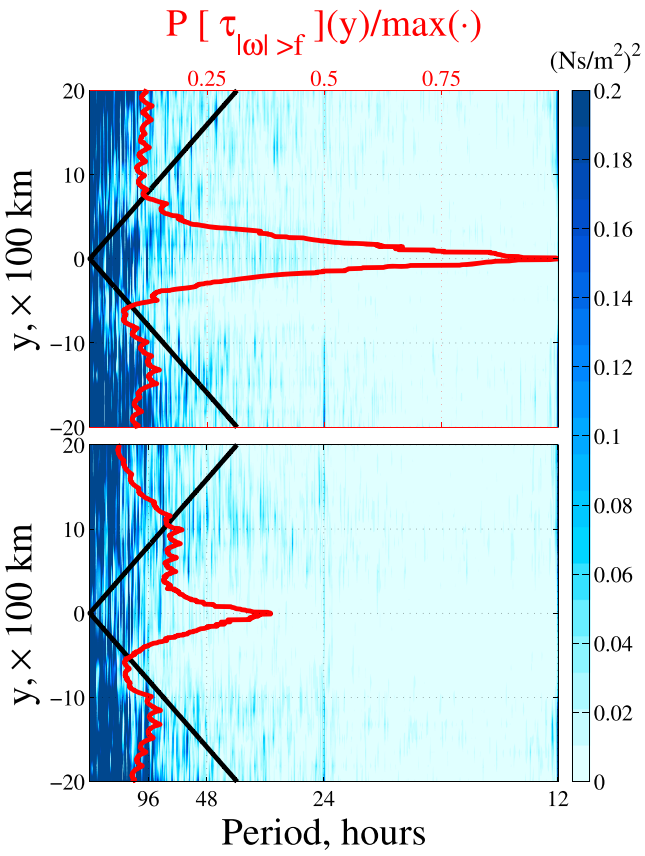

Figure 6. Temporal power spectrum of the wind stress, $P[\tau_x](\omega, y) = \left|\tau_x(\omega, y)\right|^2$. The units of $P[\tau_x](\omega, y)$ are $(\mathrm{Ns/m^2})^2$, that is, (momentum per area)^2. (upper panel) Period I (equatorial winds). (lower panel) Period II (off-equatorial winds). Solid black line in each plot separates subinertial (left of the line) and superinertial (right of the line) periods. Superinertial wind stress, $P\left[\tau_{|\omega|>|f|}\right](y) = (2\pi)^{-1}\int_{|\omega|\geq|f|} \mathrm{d}\omega\ P\left[\tau_x(\omega, y)\right]$, normalized by the maximum over all freqencies, latitudes, and both periods, is represented by the red lines. In both cases the superinertial wind stress is strongest at the equator.

the response to subinertial and superinertial forcing away from the equator in a more idealized setting of a single wind burst and show that this is indeed the case.

The meridional distribution of the superinertial wind stress can explain the observed enhancement of energy dissipation in the equatorial pycnocline qualitatively. The rate of emission of near-inertial energy from the mixed layer into the ocean interior is expected to be a decreasing function of the local Coriolis parameter, f (e.g., Balmforth & Young, 1999; D'Asaro, 1989; Zervakis & Levine, 1995). In this article we do not address the question of rate of energy loss from the mixed layer but focus on mechanisms of Froude number amplification and potential wave breaking in the ocean interior due to the three processes suggested by the model output analysis in section 3.3. In section 4 we use ray tracing and idealized single burst numerical experiments to analyze these mechanisms. To facilitate the comparison between simplified models and the full numerical simulation, we use the temporal spectral power density distribution $P[\phi](\omega, y, z)$ for any field $\phi(t, y, z)$ in the model output:

$$\phi(\omega, y, z) = \frac{1}{T}\int_0^T \mathrm{d}t\ \phi(t, y, z)\exp(-i\omega t) \tag{17a}$$

$$P[\phi](\omega, y, z) = \phi^*(\omega, y, z)\phi(\omega, y, z), \tag{17b}$$

where $T = 244$ days is the integration time period in our numerical experiments. The model output was recorded with the interval of $(\Delta t)_{\mathrm{output}} \triangleq (\Delta t)_o = 6$ hr between snapshots. This allows us to calculate spectral energy densities at frequencies $\omega_j = 2\pi j/T$, with $j = -J_o, -J_o + 1, \ldots, J_o - 1, J_o$, where $J_o = T/(2(\Delta t)_o)$. The temporal frequency resolution of the model output is $(\Delta\omega)_o = 2\pi/T$. If NIWs are generated in the mixed layer

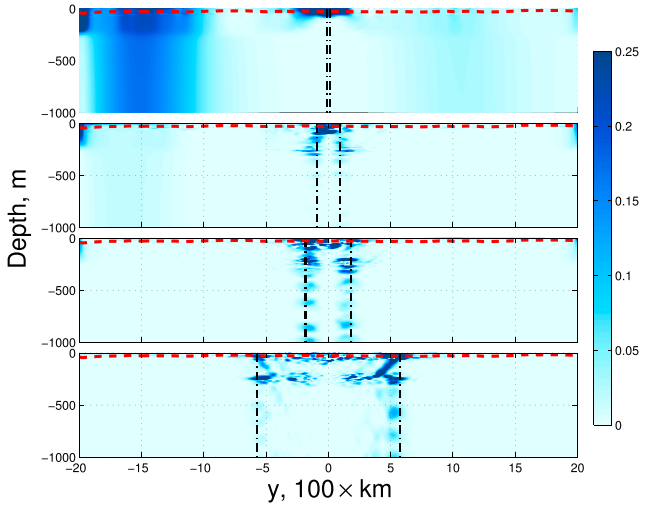

Figure 7. The normalized spectral power density distribution for the zonal velocity component, $P[u](\omega, y, z)/\max_{y,z} P[u](\omega, y, z)$ for the frequencies ω_1, ω_7, ω_{14}, and ω_{44} (from top to bottom) for the off-equatorial wind case. The dashed red line shows the time-mean mixed layer depth. The dashed black vertical lines indicate the corresponding inertial latitude $y_n = \omega_n/\beta$ for each frequency.

through the inertial pumping mechanism described in the introduction then this translates into meridional resolution $(\Delta y)_o = 2\pi/\beta T = 13$ km. The highest resolved frequency is $\omega_{J_o} = \pi/(\Delta t)_o$, and variability at a frequency ω higher that ω_{J_o} is aliased into frequency $\omega/2$. Our time series resolve local inertial periods up to latitudes $\left|y_{J_o}\right| = \pi/\left[\beta(\Delta t)_o\right] \approx 2,400$ km, which are beyond the meridional confines of the computational domain.

Figure 7 shows the power spectrum distribution of the zonal velocity component, $P[u](\omega, y, z)/\max_{y,z} P[u](\omega, y, z)$, for frequencies ω_1, ω_7, ω_{14}, and ω_{44}, with periods approximately corresponding to 244, 34.9, 17.5, and 5.5 days (from top to bottom) for the off-equatorial wind case. These periods, in turn, correspond to local inertial latitudes 13, 91, 182, and 572 km away from the equator.

At the lowest frequency shown, $\omega_1 = (\Delta\omega)_o$, the ocean response in u is strongest in a shallow region around the equator but extends to great depths south of $y = -2,000$ km. The picture is similar for other low frequencies (such as the mean flow). Since such signal is absent in the response of the meridional velocity field at these frequencies, we conclude that this variability corresponds to a forced response to the slowly varying wind field, that is, nearly geostrophic zonal currents. As such, they exhibit no meridional propagation of kinetic energy.

At somewhat higher frequencies, such as ω_7, we see an SVS response contained in the pycnocline (the second from the top panel in Figure 7). Note that there are no beams emanating from the surface at the generation latitudes, and there is no signal below the pycnocline. This may indicate that variability at this frequency is induced through nonlinear wave-wave interactions. More specifically, this scenario is consistent with the PSI of higher-frequency motion.

As we increase the frequency, the spatial character of variability changes. For ω_{14} we can clearly see an equatorially trapped wave (third panel from the top). Unlike for lower frequencies, the signal now penetrates below the pycnocline close to the equator and forms a pattern that is consistent with both equatorial trapping and a beam bouncing between turning latitudes as it propagates vertically. Note the amplification of the signal close to turning latitudes.

At high frequencies we no longer see the bouncing between turning latitudes: The beams strike the ocean bottom before encountering a turning latitude. The bottom panel in Figure 7 illustrates this for ω_{44}. The beams emanate from the base of the mixed layer in the range between about $y = 550$ and 600 km in both Southern and Northern Hemispheres off the equator, amplifying in the pycnocline and weakening on the way out of the pycnocline. There are reflections from the bottom and some hint of reflection off the turning latitudes in the ocean interior.

3.5. Summary of the Results

To summarize, we have identified four processes that may play role in the distribution of energy dissipation in the ocean interior in a simple model:

1. A more intense input of superinertial energy closer to the equator
2. Amplification via refraction through the pycnocline
3. Wave action convergence at turning latitudes for equatorially trapped waves
4. Transfer of energy to SVSs through nonlinear wave-wave interactions.

These processes will be studied in more detail in section 4.

4. Wave Amplification Mechanisms

To quantify various amplification mechanisms, we use ray tracing and the wave action balance equation to calculate the spatial distribution of wave energy density. The Froude number field, and therefore the parameterized eddy viscosity in the model, can then be calculated from the wave energy density distribution.

4.1. Wave Action Balance Equation

The general form of the wave action equation is presented in Andrews and McIntyre (1978) and Bühler (2009). Here we assume that the mean flow and waves are relatively weak and use a formulation in which mean flow-wave interactions, as well as wave-wave interactions are neglected. For a wave packet located at the point $\mathbf{x} = [y, z]$ and characterized by a wave vector $\mathbf{k} = [\ell, m]$ and wave energy density $E(\mathbf{k}, \mathbf{x}, t)$, the wave action is given by $A(\mathbf{k}, \mathbf{x}, t) = E(\mathbf{k}, \mathbf{x}, t)/\omega(\mathbf{k}, \mathbf{x})$ and governed by the wave action balance equation:

$$\frac{\partial A}{\partial t} + \frac{\partial}{\partial y}\left(c_{g,y}A\right) + \frac{\partial}{\partial z}\left(c_{g,z}A\right) + \frac{\partial}{\partial \ell}\left(r_\ell A\right) + \frac{\partial}{\partial m}\left(r_m A\right) = S, \tag{18}$$

where $c_{g,y} = \partial\omega/\partial\ell$ is the meridional group velocity of the wave packet, $c_{g,z} = \partial\omega/\partial m$ is its vertical group velocity, and $r_\ell = -\partial\omega/\partial y$ and $r_m = -\partial\omega/\partial z$ are the refraction coefficients that determine the evolution of the meridional and vertical components of the wave vector as the wave packet propagates through the environment. The right-hand side of (18) represents sources and sinks of the wave action due to forcing and dissipation.

Equation (18) is a hyperbolic partial differential equation and as such requires the initial and boundary conditions to be specified. The solution can be found by the method of characteristics.

Plane waves preserve their frequency in a time-independent medium, and the dispersion relation given by

$$\omega^2 = f^2(y) + N^2(y, z)\frac{\ell^2}{m^2} \tag{19}$$

defines characteristic hypersurfaces in the (y, z, ℓ, m) space, which are convenient to visualize as rays in the (y, z) plane, with wave vector components ℓ and m each changing along the ray.

The rays and changes in wave vector components along them can be calculated by integrating the system of ray tracing equations:

$$\dot{y} = c_{g,y} = \frac{\omega^2 - \beta^2 y^2}{\omega\ell}, \tag{20a}$$

$$\dot{z} = c_{g,z} = -\frac{\omega^2 - \beta^2 y^2}{\omega m}, \tag{20b}$$

$$\dot{\ell} = r_\ell = -\frac{\beta^2 y}{\omega} - \frac{\omega^2 - \beta^2 y^2}{2\omega}\,\frac{\partial \log N^2(y, z)}{\partial y}, \tag{20c}$$

$$\dot{m} = r_m = -\frac{\omega^2 - \beta^2 y^2}{2\omega}\,\frac{\partial \log N^2(y, z)}{\partial z}, \tag{20d}$$

where the dot denotes the differentiation with respect to time, d/dt.

4.2. Ray Tracing Into the Ocean Interior

The IGWs in our simulations are generated at the base of the mixed layer and propagate in the negative z direction until they are reflected from the bottom. It is therefore possible to eliminate time from the ray tracing equations and express the meridional location of the wave packet and its wave vector components as functions of depth. Dividing 20 by (20b) yields a system of three equations

$$\frac{\mathrm{d}y}{\mathrm{d}z} = -\frac{m}{\ell}, \tag{21a}$$

$$\frac{\mathrm{d}\ell}{\mathrm{d}z} = \frac{\beta^2 y m}{\omega^2 - \beta^2 y^2} + \frac{m}{2}\,\frac{\partial \log N^2(y, z)}{\partial y}, \tag{21b}$$

$$\frac{\mathrm{d}m}{\mathrm{d}z} = \frac{m}{2}\,\frac{\partial \log N^2(y, z)}{\partial z}. \tag{21c}$$

If the background buoyancy frequency field N^2 is independent of y, as is the initial profile in our numerical simulations, then (21c) decouples from the rest of the system and can be integrated to yield

$$m^2(z) = m^2(z_0)\frac{N^2(z)}{N^2(z_0)}, \tag{22}$$

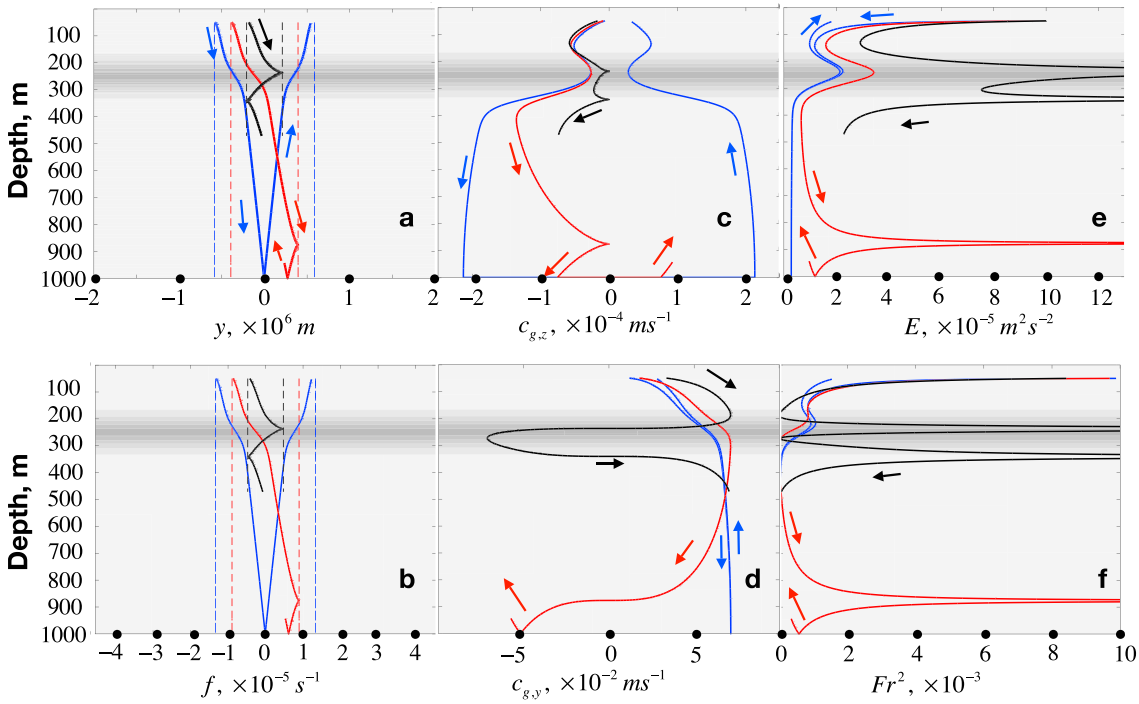

Figure 8. Various wave characteristics along ray trajectories. The lines correspond to frequencies ω_{44} (blue), ω_{29} (red), and ω_{14} (black). (a) The ray trajectories in (y, z) plane, (b) the Coriolis parameter f along trajectories, (c) vertical component of the group velocity, (d) meridional component of the group velocity, (e) wave energy density, and (f) Froude number squared associated with the wave. Arrows show the direction of time along the segment of the trajectory closest to the arrow.

where z_0 is the initial depth of the wave packet. This expression is the same as the well-known Wentzel–Kramers–Brillouin (WKB) scaling of the vertical coordinate with the background stratification for normal mode solutions but is more general because it holds for propagating wave packets and works when normal modes do not exist.

Equations (21a) and (21b) can be combined to yield the relationship between the meridional coordinate y and the meridional component of the wave vector ℓ:

$$\ell^2(y) = \ell^2(y_0)\frac{\omega^2 - \beta^2 y^2}{\omega^2 - \beta^2 y_0^2}, \tag{23}$$

which shows that as a wave packet propagates from its origin at y_0 toward the equator, the meridional scale of the wave becomes smaller.

Equations (22) and (23) can be combined to yield the following expression for the ray trajectory in the (y, z) plane.

$$\frac{sgn(y_0)}{2}\frac{\omega^2}{\beta}\left[\arcsin\frac{\beta y}{\omega} - \arcsin\frac{\beta y_0}{\omega} + \sin\left[2\arcsin\frac{\beta y}{\omega}\right] - \sin\left[2\arcsin\frac{\beta y_0}{\omega}\right]\right] = \int_{z_0}^{z} \mathrm{d}\xi \; N(\xi), \tag{24}$$

which completes the ray tracing part of solving the wave action balance equation: Given the initial position of the wave packet, $[y_0, z_0]$, the meridional position and its wave vector can first be calculated using (24), and its meridional component of the wave vector can then be determined from (23). The vertical component of the wave vector as a function of depth can be determined without the knowledge of the trajectory from (22). Rather than solve the algebraic equation (24) for y, we integrate the system of differential equations ((20a)–(20d)). We assume that the waves are emitted from just below the bottom of the mixed layer, at the meridional location where their frequency is equal to the local inertial frequency. The frequency of the wave, however, *cannot* be set exactly equal to the local inertial frequency because purely inertial waves cannot propagate. We therefore slightly detune it from the local inertial frequency to a value slightly higher than $|f|$ by setting the initial horizontal wavelength to 200 km and the initial vertical wavelength to

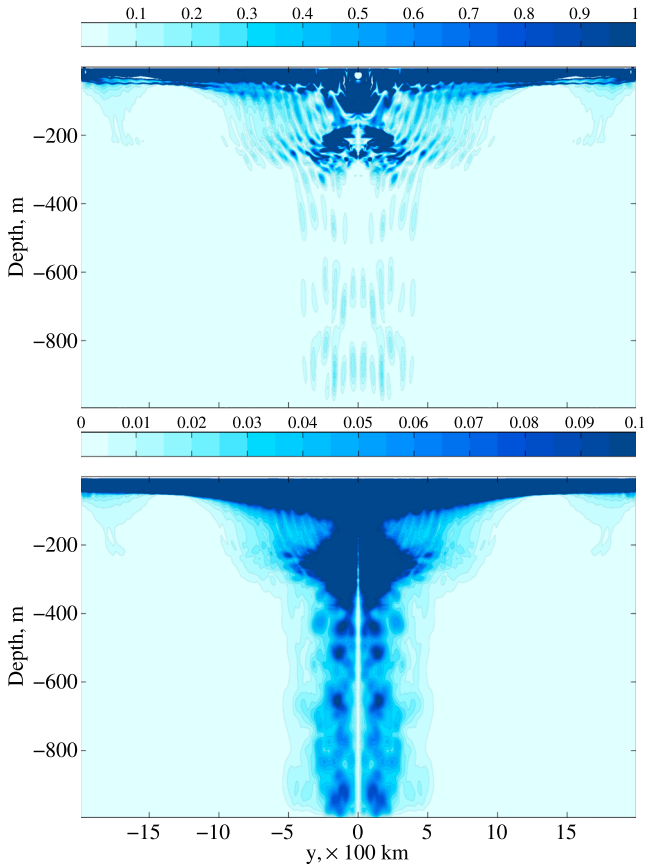

Figure 9. A snapshot (upper panel) and time-averaged (lower panel) Froude number in the uniform wind burst experiment. The snapshot is taken on Day 20. The amplification of the Froude number in the pycnocline is evident in both figures.

100 m. Although somewhat arbitrary, these settings are representative of the beam characteristics found in the numerical experiments described in section 3.

To calculate the wave energy density field, we assume that the medium is steady and the wave field is stationary. The wave action flux

$$\mathbf{F} = [F_y, F_z, F_\ell, F_m] = [c_{g,y}, c_{g,z}, r_\ell, r_m]E \tag{25}$$

is then nondivergent in the (y, z, ℓ, m) space. Integrating over an appropriately chosen control volume (We choose the control volume so that group velocity and refraction vector are parallel to sides of the control volume except for the bounding surfaces described by z =constant.) and applying the divergence theorem, that is,

$$\int_V \mathrm{d}y\mathrm{d}z d\ell\, \mathrm{d}m\ \nabla \cdot \mathbf{F} = \oint_S \mathrm{d}S \mathbf{F} \cdot \hat{\mathbf{n}}, \tag{26}$$

we obtain

$$E|_z = E|_{z_0} \frac{c_{g,z}\Big|_{z_0}}{c_{g,z}\Big|_z}, \tag{27}$$

where the subscript to the vertical bar denotes the depth at which a field is evaluated along the ray trajectory (i.e., $E|_z = E\,(y(z), z, \ell\,(z), m(z))$).

With the energy density profile known, we can also estimate the Froude number along the ray trajectory. As shown in Natarov and Richards (2019), the maximum Froude number along the beam can be expressed in

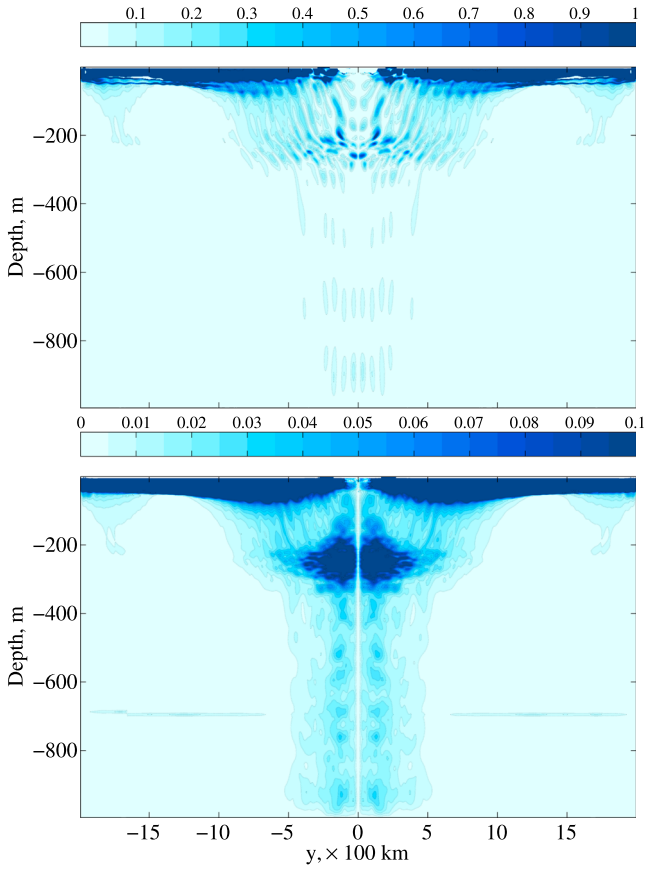

Figure 10. A snapshot (upper panel) and time-averaged (lower panel) Froude number in the almost uniform wind burst experiment. The snapshot is taken on Day 20. The amplification of the Froude number in the pycnocline is evident in both figures.

terms of the wave energy density E as

$$Fr^2 = \frac{2m^2E}{N^2}\frac{f^2}{\omega^2}\left(1 - \frac{|m|}{N}\frac{\sqrt{\omega^2 - f^2}}{\omega}\sqrt{2E}\right)^{-1} \tag{28}$$

Figure 8 traces various characteristics and fields along the beam trajectories. We chose to present the results for frequencies ω_{44} (shown in blue color in all six plots), ω_{29} (red), and ω_{14} (black). Arrows indicate the direction of time as the signal propagates along the beam. The end point of each trajectory describes the state of the wave packet after 244 days of propagation, putting an upper bound on how far from the generation site one can expect to find the wave packets of the ROMS simulations described above in section 3. Figure 8a shows the ray trajectory in the (y, z) plane. Wave packets of higher frequency propagate faster, and the ω_{44} ray have reflected from the bottom and almost reached the surface again after 244 days. However, it has not reached its turning latitude over this period of time. The ω_{14} beam, on the other hand, has only reached the depth of 300 m after 244 days but encountered turning latitudes twice along the way: first within the pycnocline and the second time just below it. The ω_{29} beam is an intermediate case, with the wave packet reaching its turning latitude once not far from the bottom.

Figure 8b shows the changes in the Coriolis parameter that a wave experiences as it propagates. The vertical dashed lines correspond to the frequencies of the waves presented in the plot. Figure 8c shows the vertical component of the group velocity. The smaller-magnitude vertical group velocity implies vertical convergence of wave energy flux and is correlated with the Froude number amplification. Figures 8e and 8f show that both refraction through pycnocline and turning latitudes lead to wave energy density and the Froude number amplification. However, the turning latitudes lead to a much stronger amplification. We therefore conclude that the most important process that leads to internal wave breaking and enhanced mixing in our simulations is the wave energy flux convergence at turning latitudes.

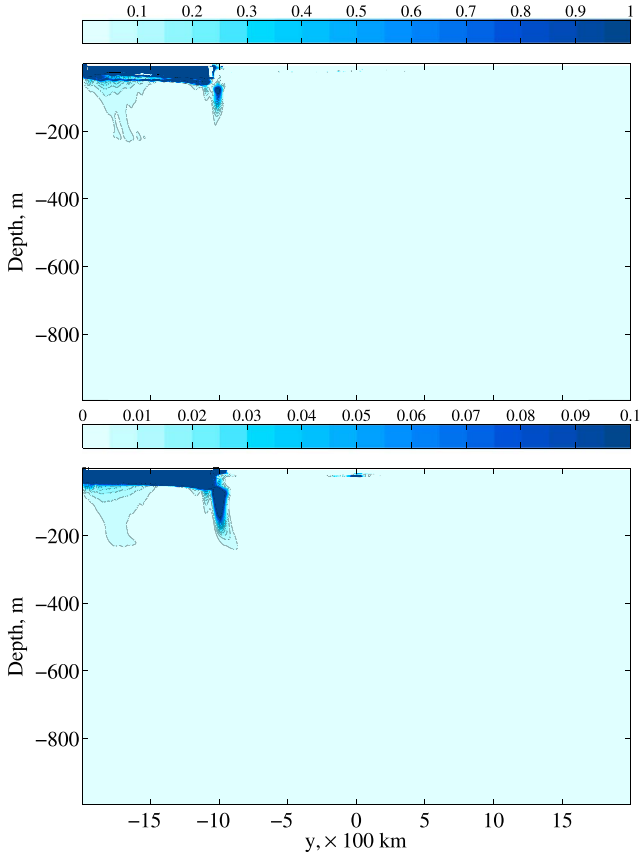

Figure 11. A snapshot (upper panel) and time-averaged (lower panel) Froude number in the subinertial off-equatorial wind burst experiment. The snapshot is taken on Day 20. There little wave activity produced in the experiment and the largest Froude number in the interior is associated with the quasi-steady jet produced at the edge of the wind patch.

4.3. Single Wind Burst Experiments

The results of the numerical experiments described in section 3 suggest that much of the ocean response to wind forcing with a complex spatial and temporal structure can be understood in terms of the ocean response to single wind events. Moreover, most of the results (i.e., equatorial trapping, Yoshida jet, and NIWs off the equator) can be explained within a linear framework. As a compliment to the experiments with observed winds, a number of idealized experiments were performed in which the ocean was forced by single wind burst events:

1. Latitudinally uniform wind burst
2. An almost uniform wind burst with forcing removed in the close neighborhood of the equator
3. A subinertial wind burst in the Southern Hemisphere
4. A superinertial wind burst in the Southern Hemisphere.

Only the results pertinent to the amplification of the Froude number are presented and discussed below.

Our modeling results presented in section 3 show that the dynamics very close to the equator is very different from the dynamics away from the equator. One unique feature of the ocean response on the equator, which is normally absent at any other meridional location, is the Yoshida jet: a strong zonal surface current induced by Ekman convergence of zonal momentum on the equator, where f changes sign. The Yoshida jet typically has its strongest magnitude directly on the equator, and this is also where its vertical shear of zonal velocity reaches largest values. Does the Yoshida jet play an important role in controlling the Froude number field in the ocean interior? To answer this questions, we compare the case of a uniform westerly wind burst, which generates a strong Yoshida jet because of strong zonal momentum convergence on the equator, and an "almost" uniform westerly wind burst, in which the wind stress is greatly reduced within a small region around the equator. Because there is essentially no wind close to the equator in the latter

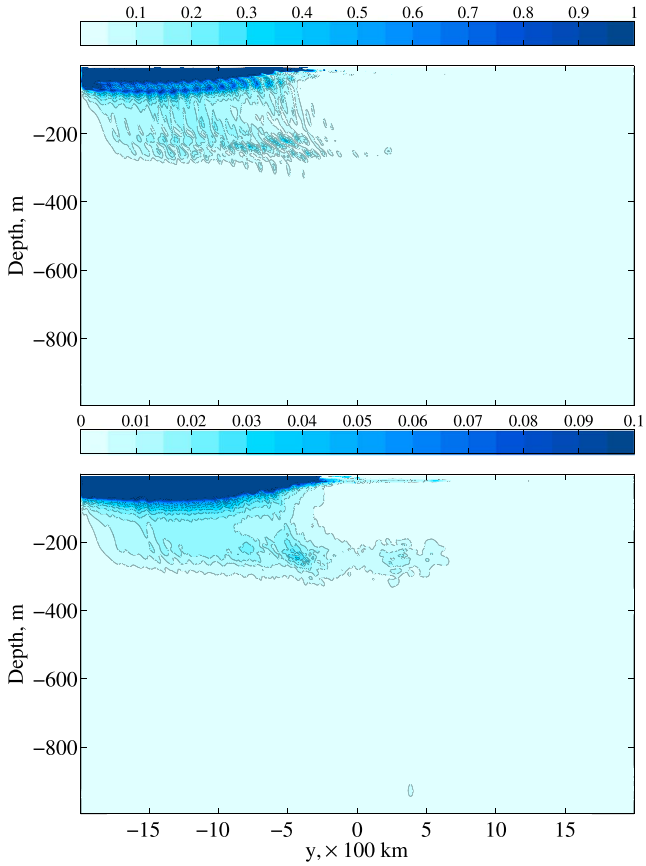

Figure 12. A snapshot (upper panel) and time-averaged (lower panel) Froude number in the short off-equatorial wind burst experiment. The snapshot is taken on Day 20. The amplification of the Froude number in the pycnocline is evident in both figures. The temporal mean figure also shows enhanced Froude number regions close to the equator associated with turning latitudes and nonlinear wave-wave interactions.

case, Ekman convergence no longer occurs directly on the equator in this setting. However, there is weaker Ekman convergence elsewhere due to the presence of a nonzero wind stress curl. The ocean response to a wind burst that is symmetric with respect to the equator is symmetric in zonal velocity u but antisymmetric in the meridional velocity v. The Yoshida jet does not have a signal in v, so it is entirely symmetric.

The resulting patterns shown in Figures 9 and 10 are very similar between the two cases away from the equator, but there are substantial differences close to the equator. Not surprisingly, the largest differences occur in the transition layer close to the equator, where the Yoshida jet is the strongest. But there are also substantial differences in the pycnocline and deeper ocean. However, these are *not* due to the Yoshida jet: Note that the Froude number is essentially 0 directly on the equator below the transition layer. The difference in the magnitude of the Froude number field is due to the fact that along with the Yoshida jet we have also removed some waves that are trapped close to the equator. The reduction in the overall Froude number is in part due to the decrease in the activity of SVSs forced directly by wind. Another factor is the reduction in the activity of SVSs created through PSI of the large scale equatorially trapped waves.

A long subinertial off-equatorial wind burst produces a strong quasi-steady jet but almost no wave activity (Figure 11). In contrast, a wind burst with a similar meridional structure but of a shorter duration produces strong off-equatorial NIWs, mixing in the off-equatorial pycnocline (Figure 12). At later stages only weak equatorially trapped waves survive.

Nonlinear wave-wave interactions can create SVSs in the absence of wind forcing (cf. d'Orgeville & Hua, 2005; Natarov et al., 2008), and while there is little mixing during later stages, there is also a slow growth of Froude number in the equatorial pycnocline. In the absence of forcing such growth can only be a result of nonlinear wave-wave interactions between equatorially trapped waves. We find that even for wind bursts

that occur far away from the equator, wave-wave interactions can be detected on a time scale of a few months. For wind bursts occurring closer to the equator we expect the effect to be much more dramatic. Returning now to the comparison between the uniform and almost uniform wind experiments described in the beginning of this section, we expect that large vertical scale equatorially trapped waves generated in the uniform wind burst experiment lose energy to SVSs through PSI. This accounts for larger Froude number close to the equator in the uniform wind burst experiment.

5. Discussion

In this paper we have demonstrated that SVS activity and energy dissipation levels are enhanced close to the equator in a simple zonally symmetric model of a tropical ocean driven by transient wind stress regardless of the distribution of temporally averaged wind power. We have established that the two main reasons for such enhancement is that the wind power spectrum is mostly superinertial near the equator and subinertial away from the equator and that enhanced mixing in the interior is mostly due to wave energy density convergence at turning latitudes. Previous studies focused on the decay of the characteristic time scale over which the mixed layer leaks its kinetic energy have with latitude (see Balmforth & Young, 1999; Zervakis & Levine, 1995). Our results are valid over a wider range of regimes and do not rely on a near-inertial approximation. We stress that determining the most important mechanism of energy emission from the mixed layer to the ocean interior was not our objective here but will be presented in a companion paper.

While waves are stronger just below the base of the mixed layer because of the above mechanism, their amplitude quickly reduces with depth as they propagate into the ocean interior because their Froude number exceeds the critical value of 4 just below the base of the mixed layer, inducing a high eddy diffusivity there. To be able to induce mixing again in the ocean interior, the fraction of waves that survive propagation through the highly diffusive region just below the base of the mixed layer have to amplify again in the ocean interior or cascade energy to smaller vertical scales. We present three different mechanisms of Froude number amplification in the ocean interior

1. Refraction through pycnocline
2. Wave action convergence at turning latitudes
3. Nonlinear wave-wave interactions.

Numerical experiments with idealized single wind bursts suggest the most important mechanism for enhanced mixing in the ocean interior is the wave action convergence at turning latitudes. While a detailed understanding of this simple problem will undoubtedly enhance our ability to interpret observations and output of more realistic models, there is a large number of phenomena that we have not addressed in this study. One alternative mechanism for generation of small vertical scale features is the flow instability. As shown in Natarov and Richards (2015), persistently high levels of mixing can be generated by the radiative instabilities of equatorial currents. The role of scattering of the internal waves off spatially complex and evolving eddy field has been addressed in Soares et al. (2016), with the results showing that eddies can dramatically influence propagation and amplification of the waves.

Acknowledgments
The work presented in this article was supported by the National Science Foundation under Grant NSF OCE07-51962 and the National Oceanic ad Atmospheric Administration under grant NA17OAR4310252. We thank two anonymous referees for constructive criticism and helpful suggestions. The details of the ROMS model setup and configuration, wind forcing, and model output can be accessed at the http://apdrc.soest.hawaii.edu website. The ERA-interim wind product used to construct the wind forcing can be found at the https://www.ecmwf.int/en/forecasts/datasets/reanalysis-datasets/era-interim website.

References

Andrews, D. G., & McIntyre, M. E. (1978). On wave action and its relatives. *Journal of Fluid Mechanics*, *89*, 647–664.
Balmforth, N. J., & Young, W. R. (1999). Radiative damping of near-inertial oscillations in the mixed layer. *Journal of Marine Research*, *57*, 561–584.
Bühler, O. (2009). *Waves and mean flows*. Cambridge: Cambridge University Press.
D'Asaro, E. A. (1989). The decay of wind-forced mixed layer inertial oscillations due to the β-effect. *Journal of Geophysical Research*, *94*(C2), 2045–2056.
d'Orgeville, M., & Hua, B. L. (2005). Equatorial inertial-parametric instability of zonally symmetric oscillating shear flows. *Journal of Fluid Mechanics*, *531*, 261–291.
Gill, A. E. (1984). On the behavior of internal waves in the wakes of storms. *Journal of Physical Oceanography*, *14*, 1129–1151.
Gregg, M. C., Peters, H., Wesson, J. C., Oakey, N. S., & Shay, T. J. (1985). Intensive measurements of turbulence and shear in the equatorial undercurrent. *Nature*, *318*, 140–144.
Howard, L. N. (1961). Note on a paper of John W. Miles. *Journal of Fluid Mechanics*, *10*, 509–512.
Large, W. G., McWilliams, J. C., & Doney, S. C. (1994). Oceanic vertical mixing: A review and a model with a nonlocal boundary layer parameterization. *Reviews of Geophysics*, *32*(4), 363–403.
McComas, C. H., & Bretherton, F. P. (1977). Resonant interactions of oceanic internal waves. *Journal of Geophysical Research*, *82*, 1397–1412.
McCreary, J. P. (1981). A linear stratified ocean model of the equatorial undercurrent. *Philosophical Transactions of the Royal Society*, *298A*, 603–635.

Miles, J. W. (1961). On the stability of heterogeneous shear flows. *Journal of Fluid Mechanics*, *10*, 496–508.
Moum, J. N., Caldwell, D. R., & Paulson, C. A. (1989). Mixing in the equatorial surface layer and thermocline. *Journal of Geophysical Research*, *94*(C2), 2005–2021.
Natarov, A., & Richards, K. J. (2009). Three-dimensional instabilities of equatorial oscillatory flows. *Journal of Fluid Mechanics*, *627*, 59–74.
Natarov, A., & Richards, K. J. (2015). Persistent presence of small vertical scale velocity features during three-dimensional equilibration of equatorial inertial instability. *Physics of Fluids*, *27*(8), 84109.
Natarov, A., & Richards, K. J. (2019). On plane internal waves: Their amplification, and potential to break in a rotating stratified quiescent fluid. *Geophysical & Astrophysical Fluid Dynamics*, *113*, 1–30. https://doi.org/10.1080/03091929.2018.1557654
Natarov, A., Richards, K. J., & McCreary, J. P. (2008). Two-dimensional instabilities of time-dependent zonal flows: Linear shear. *Journal of Fluid Mechanics*, *599*, 29–50.
Richards, K. J., Kashino, Y., Natarov, A., & Firing, E. (2012). Mixing in the western equatorial pacific and its modulation by ENSO. *Geophysical Research Letters*, *39*, L02604. https://doi.org/10.1029/2011GL050439
Richards, K. J., Natarov, A., Firing, E., Kashino, Y., Soares, S. M., Ishizu, M., et al. (2015). Shear-generated turbulence in the equatorial Pacific produced by small vertical scale flow features. *Journal of Geophysical Research: Oceans*, *120*, 3777–3791. https://doi.org/10.1002/2014JC010673
Shchepetkin, A. F., & McWilliams, J. C. (2005). The Regional Oceanic Modeling System: A split-explicit, free-surface, topography-following-coordinate ocean model. *Ocean Modelling*, *9*, 347–404.
Soares, S. M., Natarov, A., & J.Richards, K. (2016). Internal swells in the tropics: Near-inertial wave energy fluxes and dissipation during CINDY. *Journal of Geophysical Research: Oceans*, *121*, 3297–3324. https://doi.org/10.1002/2015JC011600
Staquet, C., & Sommeria, J. (2002). Internal gravity waves: From instabilities to turbulence. *Annual Review of Fluid Mechanics*, *34*, 559–593.
Stewart, R. H. (2005). *Introduction to physical oceanography*. Texas: Texas A & M University.
Sun, H., & Kunze, E. (1999). Internal wave-wave interactions. Part II: Spectral energy transfer and turbulence production. *Journal of Physical Oceanography*, *29*, 2905–2919.
Vallis, G. K. (2006). *Atmospheric and oceanic fluid dynamics.* Cambridge, U.K.: Cambridge University Press.
Zervakis, V., & Levine, M. D. (1995). Near-inertial energy propagation from the mixed layer: Theoretical considerations. *Journal of Physical Oceanography*, *25*, 2872–2889.